Near-Field Thermal Splitter Based on Magneto-Optical Nanoparticles

Wen-Xuan Ge(葛文宣)[1,2,3,4], Yang Hu(胡杨)[4,5], Lei Gao(高雷)[1,2,3*], and Xiaohu Wu(吴小虎)[4*]

[1]*School of Physical Science and Technology & Collaborative Innovation Center of Suzhou Nano Science and Technology, Soochow University, Suzhou 215006, China*
[2]*School of Optical and Electronic Information, Suzhou City University, Suzhou 215104, China*
[3]*Jiangsu Key Laboratory of Thin Films, Soochow University, Suzhou 215006, China*
[4]*Shandong Institute of Advanced Technology, Jinan 250100, China*
[5]*School of Power and Energy, Northwestern Polytechnical University, Xi'an 710072, China*

(Received 25 July 2023; accepted manuscript online 26 September 2023)

Based on the many-body radiative heat transfer theory, we investigate a thermal splitter based on three magneto-optical InSb nanoparticles. The system comprises a source with adjustable parameters and two drains with fixed parameters. By leveraging the temperature and magnetic field dependence of the permittivity of InSb, the direction of heat flux in the system can be controlled by adjusting the magnetic field or temperature at the source. Under magnetic field control, the coupling between the separated modes, and the suppression of the zero-field mode induced by the magnetic field, are utilized to achieve a thermal splitting ratio within the modulation range of 0.15–0.58. Furthermore, temperature control results in a thermal splitting ratio ranging from 0.15 to 0.99, as a result of the suppression of the zero-field mode by the magnetic field and the blue shift effect of the zero-field mode frequency increasing with temperature. Notably, the gap distance between nanoparticles does not significantly affect the splitting ratio. These findings provide valuable theoretical guidance for utilizing magneto-optical nanoparticles as thermal splitters and lay the groundwork for implementing complex heat flux networks using InSb for energy collection and heat transfer control.

DOI: 10.1088/0256-307X/40/11/114401

The theory of near-field radiative heat transfer (NFRHT) predicts that heat flux can surpass the blackbody radiation limit at scales smaller than the thermal characteristic wavelength. Moreover, photon-based heat flux transfer in NFRHT can be significantly faster than phonon-based heat transfer.[1–5] These characteristics have attracted considerable interests in utilizing NFRHT for information processing. In 2010, Otey *et al.* proposed the concept of a near-field thermal diode, analogous to an electric diode, enabling control over the direction of heat flux propagation.[6] This breakthrough inspired the development of numerous nanoscale thermal devices, such as near-field transistors,[7,8] modulators,[9–11] repeaters[12,13] and splitters.[14–16] A thermal splitter is a device capable of directing the propagation of heat flux exchanged between terminals. One simple design for a thermal splitter, introduced by Ben-Abdallah *et al.*,[14] consists of three terminals: a source and two drains. By manipulating the Fermi levels in graphene nano-disks, the heat flux can be controlled to propagate from the source to one of the drains as desired. Based on the work of Ben-Abdallah *et al.*, Song *et al.* achieved a high-contrast modulator and a thermal splitter with a splitter ratio exceeding 99% using graphene/SiC core–shell nanoparticles (NPs).[15] Guo *et al.* utilized tunability and inhomogeneity in Weyl semimetals to achieve a high splitting ratio, which can be tuned by controlling the Weyl nodes with an external field.[16] In addition to the graphene and Weyl semimetals, magneto-optical materials also exhibit permittivity that can be regulated by external magnetic fields, which holds significant value for discussions on thermal splitters.

InSb, as a magneto-optical material, finds widespread applications in NFRHT due to its support to a temperature-dependent optical resonance mode in the mid-infrared band. In the case of two-body systems, thermal diodes utilizing InSb are commonly observed.[17,18] By selecting a suitable temperature difference and adjusting the external magnetic field, Wang and Gao[19] realized a thermal diode with adjustable rectification efficiency over a wide range. Additionally, Ogundare *et al.*[20] achieved a diode with large rectification efficiency, even under conditions of small temperature differences, by investigating the nonlocal effect of InSb NPs. In the case of many-body systems, the circular heat flux around InSb NPs due to the presence of magnetic fields can lead to observation of the thermal Hall effect.[21] Specifically, when a constant magnetic field is applied, the heat flux exists in the direction perpendicular to the primary temperature gradient. Furthermore, exploring the periodic magnetic field on InSb NPs enables the achievement of a heat pump effect, allowing for the acceleration or deceleration of heat flux transfer.[22] On the basis of the magnetically adjustable and temperature-dependent optical properties of InSb, we propose a near-field thermal splitter (Fig. 1) consisting of

*Corresponding authors. Email: leigao@suda.edu.cn; xiaohu.wu@iat.cn
© 2023 Chinese Physical Society and IOP Publishing Ltd

three InSb NPs. Our findings demonstrate that efficient thermal splitting can be achieved by modulating the external magnetic field and the temperature of the InSb NPs.

In this Letter, we first briefly review the optical property of magneto-optical material InSb relevant to NFRHT. Then, we present the numerical results of the designed near-field thermal splitter. Finally we provide our conclusions.

Models and Methods. To demonstrate the method of operation and splitting effects of our thermal splitter, we analyze a configuration consisting of three magneto-optical InSb NPs with radius $R = 20\,\text{nm}$, as shown in Fig. 1. Here, the subscript i is employed to indicate the temperature, magnetic field or optical modes associated with particle i, and subscript ij is used to indicate the heat flux transfer from particle i to particle j. For simplicity, we assume that the centers of these NPs align within the same plane. The distance between NP_1 and NP_2 is set as $l = 8R$. NP_3 is located on the mid-perpendicular line of NP_1 and NP_2, with a vertical distance of $d = \sqrt{3}R$. These parameters ensure that the NPs satisfy the dipolar approximation and can be treated as point sources.[23]

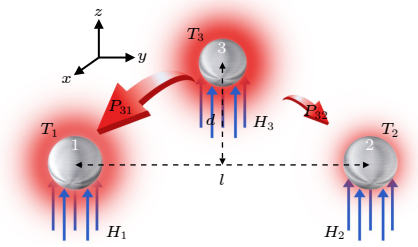

Fig. 1. Schematic of a thermal splitter. Three InSb nanoparticles (NPs) with different magnetic fields and temperatures exchange thermal energy in the near-field through many-body interactions. The magnitude of heat flux can be controlled by appropriate tuning of the magnetic field or temperature of the top particle (NP_3).

When a magnetic field is applied in the direction parallel to the z-axis, the permittivity tensor $\bar{\bar{\varepsilon}}$ of InSb NPs takes the form[21]

$$\bar{\bar{\varepsilon}} = \begin{pmatrix} \varepsilon_1 & -i\varepsilon_2 & 0 \\ i\varepsilon_2 & \varepsilon_1 & 0 \\ 0 & 0 & \varepsilon_3 \end{pmatrix}, \tag{1}$$

with

$$\begin{aligned} \varepsilon_1(H) &= \varepsilon_\infty \Big[1 + \frac{\omega_\text{L}^2 - \omega_\text{T}^2}{\omega_\text{T}^2 - \omega^2 - i\Gamma\omega} + \frac{\omega_\text{p}^2(\omega + i\gamma)}{\omega[\omega_\text{c}^2 - (\omega + i\gamma)^2]}\Big], \\ \varepsilon_2(H) &= \frac{\varepsilon_\infty \omega_\text{p}^2 \omega_\text{c}}{\omega[(\omega + i\gamma)^2 - \omega_\text{c}^2]}, \\ \varepsilon_3 &= \varepsilon_\infty \Big[1 + \frac{\omega_\text{L}^2 - \omega_\text{T}^2}{\omega_\text{T}^2 - \omega^2 - i\Gamma\omega} - \frac{\omega_\text{p}^2}{\omega(\omega + i\gamma)}\Big], \end{aligned} \tag{2}$$

where $\varepsilon_\infty = 15.75$ is the infinite-frequency permittivity, $\omega_\text{L} = 3.62 \times 10^{13}\,\text{rad/s}$, $\omega_\text{T} = 3.39 \times 10^{13}\,\text{rad/s}$ and $\Gamma = 5.65 \times 10^{11}\,\text{rad/s}$ are the parameters of the phonon contribution.[24] The heat flux splitting effect primarily arises from the carrier contribution in InSb, with a plasma frequency of free carriers denoted as $\omega_\text{p} = \sqrt{n(T)e^2/m^*\varepsilon_0}$ and phenomenological scattering rate represented by $\gamma = e/m^*\mu(T)$, where the electron effective mass is given by $m^* = 0.015m_\text{e}$, and m_e is the static mass of an electron. The temperature-dependent carrier mobility $\mu(T)$ (in $\text{m}^2/\text{V·s}$) and the carrier density $n(T)$ (in m^{-3}) are defined as[17]

$$\mu(T) = 7.7 \times \Big(\frac{T}{300}\Big)^{-1.66}, \tag{3}$$

$$\begin{aligned} n(T) =& 2.9 \times 10^{17}(2400 - T)^{0.75}(1 + 2.7 \times 10^{-4}T) \\ &\times T^{1.5} \exp\Big(-\frac{0.129 - 1.5 \times 10^{-4}T}{k_\text{B}T}\Big). \end{aligned} \tag{4}$$

The cyclotron frequency $\omega_\text{c} = eH/m^*$ arises from the presence of an external magnetic field H. For the particles size we investigated, it is necessary to add nanoscale magnetic fields, which can be achieved by utilizing nanomagnet arrays or metal ring.[25,26] If the external magnetic field is absent ($H = 0\,\text{T}$), the InSb NPs exhibit optical isotropy with a permittivity $\varepsilon = \varepsilon_3$.

The NFRHT from $\text{NP}_{\boldsymbol{j}}$ to $\text{NP}_i (T_j > T_i)$ can be described as[27,28]

$$P_{ij} = 3\int_0^{+\infty} \frac{d\omega}{2\pi}\big[\Theta(\omega, T_j) - \Theta(\omega, T_i)\big]\tau_{ij}(\omega), \tag{5}$$

where $\Theta(\omega, T) = \hbar\omega/[\exp(\hbar\omega/k_\text{B}T) - 1]$ is the mean energy of a Planck oscillator, $\hbar$ is the reduced Planck constant, and k_B is the Boltzmann constant. Here, $\tau_{ij}(\omega)$ is the transmission coefficient between NP_i and $\text{NP}_{\boldsymbol{j}}$, with[29,30]

$$\tau_{ij}(\omega) = \frac{4}{3}k_0^4 \text{Tr}[\bar{\bar{\chi}}_i \bar{\bar{G}}_{ij} \bar{\bar{\chi}}_j \bar{\bar{G}}_{ij}^\dagger], \tag{6}$$

where $k_0 = \omega/c$ is the vacuum wavevector, $\bar{\bar{\chi}}_i = (\bar{\bar{\alpha}}_i - \bar{\bar{\alpha}}_i^\dagger)/2i$ is the response function of NP_i, $\bar{\bar{\alpha}}_i = 4\pi R^3 \times (\bar{\bar{\varepsilon}}_i - \bar{\bar{I}})/(\bar{\bar{\varepsilon}}_i + 2\bar{\bar{I}})$ is the polarizability tensor in Clausius–Mossoti form,[31,32] with $\bar{\bar{I}}$ being the unit matrix and $\bar{\bar{\varepsilon}}_i$ the permittivity tensor of NP_i. For a three-body NP system, considering many-body interactions, the coupling matrix $\bar{\bar{G}}_{ij}$ reads[27,30]

$$\begin{aligned} \bar{\bar{G}}_{ij} &= \bar{\bar{D}}_{ijk}^{-1}[\bar{\bar{G}}_{0,ij} + k_0^2 \bar{\bar{B}}_{ijk} \bar{\bar{D}}_{kj}^{-1} \bar{\bar{G}}_{0,kj}], \\ \bar{\bar{D}}_{ijk} &= \bar{\bar{D}}_{ij} - k_0^4 \bar{\bar{B}}_{ijk} \bar{\bar{D}}_{kj}^{-1} \bar{\bar{B}}_{kji}, \\ \bar{\bar{B}}_{ijk} &= \bar{\bar{G}}_{0,ik} \bar{\bar{\alpha}}_k + k_0^2 \bar{\bar{G}}_{0,ij} \bar{\bar{\alpha}}_j \bar{\bar{G}}_{0,jk} \bar{\bar{\alpha}}_k, \end{aligned} \tag{7}$$

where $\bar{\bar{D}}_{ij} = \bar{\bar{I}} - k_0^4 \bar{\bar{G}}_{0,ij} \bar{\bar{\alpha}}_j \bar{\bar{G}}_{0,ji} \bar{\bar{\alpha}}_i$ is the coupling matrix of the two-body NP system and $\bar{\bar{G}}_{0,ij}$ is the vacuum Green function, which is a function of the position of the NPs,[19]

$$\begin{aligned} \bar{\bar{G}}_{0,ij} = \frac{e^{ik_0 r_{ij}}}{4\pi r_{ij}} \Big[\Big(1 + \frac{ik_0 r_{ij} - 1}{k_0^2 r_{ij}^2}\Big)\bar{\bar{I}} \\ + \frac{3 - 3ik_0 r_{ij} - k_0^2 r_{ij}^2}{k_0^2 r_{ij}^2} \hat{r}_{ij} \otimes \hat{r}_{ij}\Big], \end{aligned} \tag{8}$$

where $r_{ij} = |\boldsymbol{r}_{ij}|$ is the magnitude of the vector linking two NPs, $\hat{r}_{ij} = \boldsymbol{r}_{ij}/r_{ij}$, and $\otimes$ is the outer product.

To provide a qualitative description of the operational effect of our device, the split ratio is defined as $P_{31}/(P_{31} + P_{32})$.[14] When this ratio is equal to 1 (0), it indicates that the heat flux is entirely transferred from NP_3 to NP_1 (NP_2). A split ratio of 0.5 signifies an equal distribution of heat flux from NP_3 to the other two particles.

Here we aim to achieve the flexibility of adjusting the parameters on NP_3 to freely vary the split ratio within the range of 0 to 1. This capability allows for control of the operating state of the splitter.

Results and Discussion. Let us consider a specific case where a magnetic field is applied along the z-axis on NP_1 and NP_3, while NP_2 remains unaffected by any magnetic field, as depicted in the inset of Fig. 2(a). The magnetic field H_1 maintains a constant value of 2 T, while H_3 varies within the range of 0–6 T. In this case, we assume the temperature of NP_3 (T_3) to be 301 K, whereas T_1 and T_2 are both set to 300 K. These temperature parameters ensure the existence of a heat flux from NP_3 to the other two particles while prohibiting any heat transfer between NP_1 and NP_2. In addition, this temperature configuration avoids frequency shifts in the optical mode. Thus one can focus on discussing the impact of the magnetic field on the system. In the following discussion, the solid (dashed) line represents the heat flux power P_{ij} and transmission coefficient τ_{ij} between NP_1 (NP_2) and NP_3. As can be seen from the left axis in Fig. 2(a), the heat flux power P_{32} initially exhibits a sharp decline as H_3 increases. However, once H_3 surpasses 2 T, P_{32} converges to a constant value of 1.5×10^{-15} W. On the other hand, the value of P_{31} reaches its maximum when $H_3 = H_1 = 2$ T. Otherwise, it consistently hovers around 1.5×10^{-15} W with variations in the magnetic field. Consequently, when $H_3 = 0$ T, the split ratio reaches its minimum value of 0.15, indicating that 85% of the heat flux transfers from NP_3 to NP_2. In contrast, when $H_3 = 2$ T, the split ratio achieves its maximum value of 0.58, implying that 58% of the heat flux is directed to NP_1. Notably, when H_3 exceeds 2 T, the splitter exhibits minimal regulation over the heat flux with $P_{31}/(P_{31}+P_{32})$ maintained at 0.5. This operational range of 0.15–0.58 is unfavorable for a thermal splitter.

In order to improve the performance of our thermal splitter, we now analyze the underlying physical mechanism with the transmission coefficient τ_{ij}. In Fig. 2(b), $H_1 = 2$ T and $H_2 = 0$ T are fixed and three special cases of $H_3 = 0$, 2, and 4 T are selected for analyses. In Fig. 2(b), we use Arabic numerals (i) and Roman numerals (I, Ⅱ, Ⅲ) to denote different optical modes supported on the ith particle. By solving for the case where the denominator of the polarizability $\boldsymbol{\alpha}_i$ becomes zero, the frequency positions of these three modes can be determined as follows:[19,24]

$$\begin{aligned}&\omega_{\mathrm{I}}(T),\ \mathrm{Re}(\varepsilon_3+2)=0,\\ &\omega_{\mathrm{II}}(T,H),\ \mathrm{Re}[(\varepsilon_1+2)+\varepsilon_2]=0,\\ &\omega_{\mathrm{III}}(T,H),\ \mathrm{Re}[(\varepsilon_1+2)-\varepsilon_2]=0,\end{aligned}\tag{9}$$

where mode I is the zero-field mode whose frequency does not change with the magnetic field, while modes Ⅱ and Ⅲ are the separated modes depend on the intensity of the magnetic field. When the applied magnetic field is 0, it can be observed that $\omega_{\mathrm{I}} = \omega_{\mathrm{II}} = \omega_{\mathrm{III}}$, indicating that the separated modes disappear. Note that all these mode frequencies are strongly dependent on temperature. Notably, when the modes of NP_3 coincide in frequency with the modes of NP_1 or NP_2, we use the color red to indicate their coupling and no longer label these modes of NP_3 in Fig. 2(b).

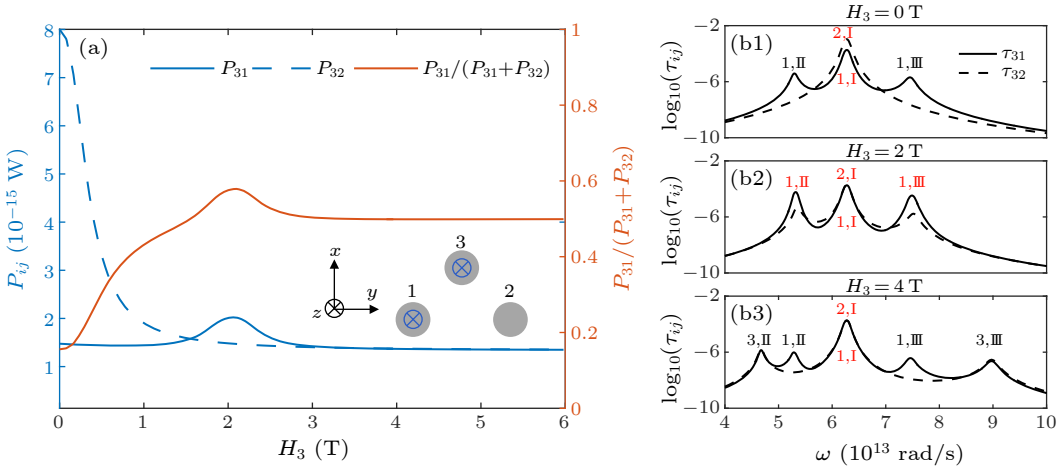

Fig. 2. (a) Left vertical axis: heat flux power P_{31} from NP_3 to NP_1 (solid blue line) and P_{32} from NP_3 to NP_2 (dashed blue line) versus the magnetic field applied on NP_3. Right vertical axis: corresponding thermal split ratio (orange line) defined as $P_{31}/(P_{31}+P_{32})$. (b) Transmission coefficient τ_{ij} of different P_{ij} with (b1) $H_3 = 0$ T, (b2) $H_3 = 2$ T, and (b3) $H_3 = 4$ T, while $H_1 = 2$ T, $H_2 = 0$ T, $T_1 = T_2 = 300$ K, and $T_3 = 301$ K. Markings with Arabic numerals represent NPs and Roman numerals represent modes. Red markings indicate mode coupling between NP_3 and NP_1 or NP_2. The legend in (b1) also applies to the other figures in (b).

By comprehensively observing three images in Fig. 2(b), it can be seen that the frequencies with resonant modes correspond to the peak values of the transmission coefficient. Moreover, when there is mode coupling between two NPs (marked in red), the transmission coefficient at the coupling frequency can increase by three orders of magnitude compared with the case without coupling (marked in black), and by six orders of

magnitude compared with the case without any mode. This demonstrates that the coupling between resonant modes dominates the heat transfer in our system. Further analysis focuses on understanding the minimum ratio of 0.15 observed when $H_3 = 0\,\mathrm{T}$ in Fig. 2(b1). In this scenario, both NP_2 and NP_3 lack a magnetic field, and solely support mode I. The coupling between them results in the dashed line in Fig. 2(b1), exhibiting a peak at $\omega_{2,\mathrm{I}}(300\,\mathrm{K}) \approx \omega_{3,\mathrm{I}}(301\,\mathrm{K}) = 6.27 \times 10^{13}\,\mathrm{rad/s}$. Introducing an external magnetic field $H_1 = 2\,\mathrm{T}$ to NP_1 induces two smaller peaks in its transmission coefficient at $\omega_{1,\mathrm{II}}(300\mathrm{K}, 2\,\mathrm{T}) = 5.29\times10^{13}\,\mathrm{rad/s}$ and $\omega_{1,\mathrm{III}}(300\,\mathrm{K}, 2\,\mathrm{T}) = 7.46\times10^{13}\,\mathrm{rad/s}$. Since NP_3 does not have any mode coupling with NP_1 at these two frequencies, the peaks of τ_{31} corresponding to these frequencies are small. Simultaneously, due to the existence of separated modes II and III, the zero-field mode I is suppressed, resulting in the peak value of τ_{31} at $6.27 \times 10^{13}\,\mathrm{rad/s}$ being one order of magnitude smaller than that of τ_{32}. Specifically, the suppression of certain modes occurs for the following reason. In the absence of a magnetic field, InSb supports mode I in all three axes. However, when a magnetic field is applied along the z-axis, InSb supports mode I only in the z-axis, as indicated by Eq. (1). Consequently, $P_{32} \gg P_{31}$ and the split ratio reaches its minimum of 0.15. In Fig. 2(b2), when $H_3 = 2\,\mathrm{T}$, modes I, II, and III supported on NP_3 can couple with the three modes on NP_1, resulting in τ_{31}, exhibiting three peaks at $\omega_{1,\mathrm{II}}(300\,\mathrm{K}, 2\,\mathrm{T}) = 5.29 \times 10^{13}\,\mathrm{rad/s}$, $\omega_{1,\mathrm{I}}(300\,K) = 6.27 \times 10^{13}\,\mathrm{rad/s}$, and $\omega_{1,\mathrm{III}}(300\,\mathrm{K}, 2\,\mathrm{T}) = 7.46 \times 10^{13}\,\mathrm{rad/s}$. However, NP_2 does not support modes at $5.29\times10^{13}\,\mathrm{rad/s}$ and $7.46\times10^{13}\,\mathrm{rad/s}$, causing the value of τ_{32} at these frequencies to be significantly smaller than τ_{31}. Unfortunately, due to the weak gyrotropic response of InSb,[16,33,34] the coupling value of the separated modes is still one order of magnitude smaller than the coupling value of mode I. As a result, the maximum achievable ratio is only 0.58. When $H_3 = 4\,\mathrm{T}$, the three NPs can only couple at $\omega_{\mathrm{I}}(300\,\mathrm{K})$ in Fig. 2(b3). Although there are peaks at other mode frequencies, they are considerably smaller than the peak value under coupling. Consequently, when the magnetic field exceeds 2 T, the heat flux powers P_{31} and P_{32} become almost equal, leading to a ratio that can only reach 0.5. However, the frequency of the type-I mode of InSb magneto-optical NPs remains unchanged with variations in the magnetic field. This means that, no matter how we adjust the external magnetic field, the modes on NP_1 and NP_3, as well as NP_2 and NP_3, always couple at $\omega_{\mathrm{I}}(\mathrm{T})$. The existence of this coupling results in P_{31} and P_{32} being less susceptible to changes in the magnetic field. Consequently, the splitter only has a split ratio between 0.15 and 0.58, and fails to achieve a satisfactory level of performance.

Next, we explore the variation of the split ratio with magnetic field H_3 in Fig. 3 while keeping H_1 at different fixed values. When $H_1 = H_2 = 0\,\mathrm{T}$, since the parameters of NP_1 and NP_2 are completely consistent, $P_{32} = P_{31}$ remains unchanged with H_3. As a result, the device lacks adjustable split capability. When an external magnetic field is applied to NP_1, the maximum split ratio is observed at $H_1 = H_3$, and the corresponding maximum value remains nearly constant at approximately 0.58 for different values of H_1. Furthermore, when the magnetic field H_3 is set to 0 T, the minimum ratio remains around 0.15 regardless of the magnitude of H_1 (as long as it is not zero). As mentioned above, the presence of mode I coupling between NPs, independent of magnetic fields, results in maximum and minimum values that hardly vary with H_1. Additionally, the inset in Fig. 3 depicts the variation of the split ratio with H_2 while keeping $H_1 = H_3 = 0\,\mathrm{T}$. As H_2 increases from 0 T to 2 T, the split ratio can be enhanced from 0.5 to 0.85. However, as H_2 continues to increase, the split ratio tends to approach a constant value. This demonstrates that adjusting the magnetic field on NP_2 alone can achieve unidirectional heat transfer from NP_3 to NP_1. However, modifying H_2 alone cannot achieve unidirectional heat transfer from NP_3 to $NP_1(P_{31}/(P_{31} + P_{32}) < 0.5)$. The results presented in Figs. 2 and 3 illustrate that InSb magneto-optical NPs cannot be employed to realize high performance, regulated thermal splitters by solely adjusting the magnitude of the magnetic field.

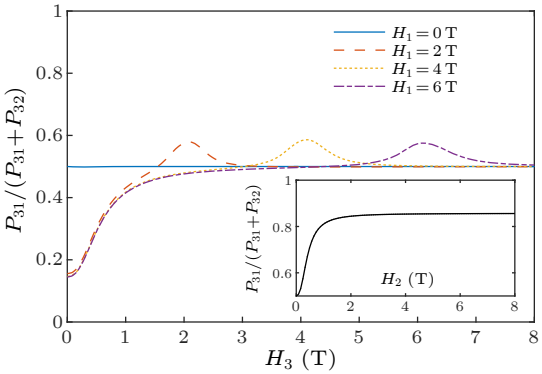

Fig. 3. Thermal split ratio as a function of magnetic field H_3 on NP_3 for $H_1 = 0\,\mathrm{T}$, $H_1 = 2\,\mathrm{T}$, $H_1 = 4\,\mathrm{T}$, and $H_1 = 6\,\mathrm{T}$, with $H_2 = 0\,\mathrm{T}$, $T_1 = T_2 = 300\,\mathrm{K}$, and $T_3 = 301\,\mathrm{K}$. The inset shows the thermal split ratio as a function of H_2 with $H_1 = H_3 = 0\,\mathrm{T}$.

To improve performance of the thermal splitter, we investigate the influence of temperature changes on our system. In Fig. 4, with $H_1 = 2\,\mathrm{T}$, $H_2 = H_3 = 0\,\mathrm{T}$, and $T_1 = T_2 = 300\,\mathrm{K}$, we observe the changes in heat flux power and split ratio with temperature T_3 on NP_3. Here, solid (dashed) lines represent the heat flux power P_{ij} and the transmission coefficient τ_{ij} between NP_1 (NP_2) and NP_3. As T_3 increases, P_{32} reaches a maximum value near $T_3 = 301\,\mathrm{K}$, while P_{31} reaches a maximum value near $T_3 = 318\,\mathrm{K}$. By varying the temperature on NP_3 from 301 K to 318 K, the split ratio can be smoothly adjusted from 0.15 to 0.95. Although this is still not as high as the 99% : 1% achieved by other thermal splitters,[14–16] it represents a significant improvement over the results shown in Figs. 2 and 3. Figure 4(b) provides a clear explanation of the physical mechanism underlying the thermal splitter achieved by temperature variation. Here, the color

red is utilized to indicate the coupling between the displayed mode and the mode on NP_3. The results presented in Fig. 4(b1) are identical to those depicted in Fig. 2(b1), and the earlier discussion in Fig. 2(b1) provides an explanation for the observed minimum split ratio of 0.15, which can be explained by the suppression of mode I with magnetic field. Next, in Fig. 4(b2), as the temperature T_3 increases to 318 K, mode I on NP_3 undergoes a blue shift. This shift causes $\omega_{3,\mathrm{I}}(318\,\mathrm{K})$ to align with the frequency of mode Ⅲ on NP_1 induced by H_1, that is, $\omega_{3,\mathrm{I}}(318\,\mathrm{K}) = \omega_{1,\mathrm{III}}(300\,\mathrm{K}, 2\,\mathrm{T})$. This leads to coupling between these two modes, resulting in a peak value of τ_{31} at $\omega_{1,\mathrm{III}}(300\,\mathrm{K}, 2\,\mathrm{T}) = 7.46 \times 10^{13}$ rad/s in Fig. 4(b2). However, this frequency of mode I on NP_3 significantly deviates from the frequency of mode I on NP_2, which is $\omega_{2,\mathrm{I}}(300\,\mathrm{K}) = 6.27 \times 10^{13}$ rad/s, causing only two smaller peaks in τ_{32}. Consequently, P_{31} becomes larger than P_{32}, resulting in a split ratio of 0.95 at $T_3 = 318\,\mathrm{K}$. We also discuss the situation when the temperature $T_3 = 340\,\mathrm{K}$, as shown in Fig. 4(b3). In this case, there is no mode coupling observed among the three NPs. As a result, there is only a slight difference between P_{32} and P_{31}, leading to a split ratio of approximately 0.6.

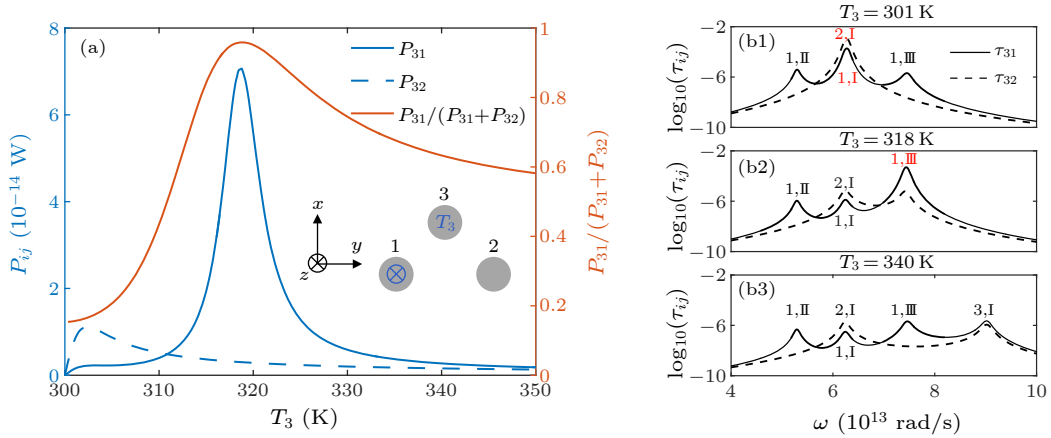

Fig. 4. (a) Left vertical axis: heat flux power P_{31} from NP_3 to NP_1 (solid blue line) and P_{32} from NP_3 to NP_2 (dashed blue line) versus temperature of NP_3. Right vertical axis: corresponding thermal split ratio (orange line) defined as $P_{31}/(P_{31} + P_{32})$. (b) Transmission coefficient τ_{ij} for different heat flux powers with (b1) $T_3 = 301\,\mathrm{K}$, (b2) $T_3 = 318\,\mathrm{K}$, and (b3) $T_3 = 340\,\mathrm{K}$, with $H_2 = H_3 = 0\,\mathrm{T}$, $H_1 = 2\,\mathrm{T}$, and $T_1 = T_2 = 300\,\mathrm{K}$. Markings with Arabic numerals represent particles and Roman numerals represent modes. Red markings indicate mode coupling between NP_3 and the displaced modes of NP_1 or NP_2. The legend in (b1) also applies to the other panels in (b).

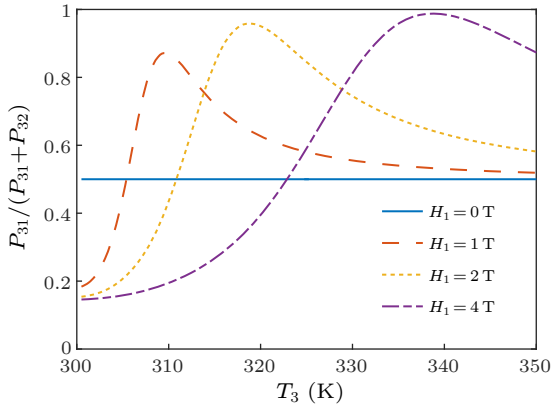

Fig. 5. Thermal split ratio as a function of temperature T_3 of NP_3 for the cases of $H_1 = 0\,\mathrm{T}$, $H_1 = 1\,\mathrm{T}$, $H_1 = 2\,\mathrm{T}$, and $H_1 = 4\,\mathrm{T}$, with $H_2 = H_3 = 0\,\mathrm{T}$ and $T_1 = T_2 = 300\,\mathrm{K}$.

Figure 5 further investigates the dependence of the split ratio on T_3 when H_1 has different fixed values. Throughout the analysis, H_2 and H_3 are maintained at 0 T, and T_1 and T_2 are kept at 300 K. When $H_1 = 0\,\mathrm{T}$, the parameters of NP_1 and NP_2 are identical, resulting in a fixed split ratio of 0.5 irrespective of any temperature fluctuations on NP_3. As H_1 increases, the range of achievable ratios expands. Specifically, it extends from 0.19–0.85 at $H_1 = 1\,\mathrm{T}$ to 0.15–0.99 at $H_1 = 4\,\mathrm{T}$. Regardless of the value of H_1, excluding $H_1 = 0\,\mathrm{T}$, the minimum split ratio consistently occurs at $T_3 = 301\,\mathrm{K}$. As the intensity of mode I on NP_1 decreases with the increase of H_1, when H_1 increases from 1 T to 4 T, the P_{31} controlled by mode I coupling decreases while P_{32} remains unchanged, and the corresponding minimum ratio decreases from 0.19 to 0.15. On the other hand, as H_1 increases, the maximum ratio is observed at higher values of T_3. This behavior can be attributed to the increase in frequency $\omega_{1,\mathrm{III}}(300\,\mathrm{K}, H_1)$ with increasing H_1. Hence, a higher T_3 is required to support a type-I mode with a larger frequency, $\omega_{3,\mathrm{I}}(T_3)$, to couple with this mode Ⅲ on NP_1. Simultaneously, this shift in frequency $\omega_{3,\mathrm{I}}(T_3)$ causes the mode I on NP_3 to move away from mode I on NP_2 at $\omega_{2,\mathrm{I}}(300\,\mathrm{K}) = 6.27 \times 10^{13}$ rad/s. As a result, the interference from mode I coupling in the heat flux is diminished, leading to a split ratio approaching 0.99 at $T_3 = 338\,\mathrm{K}$ when $H_1 = 4\,\mathrm{T}$. This observation underscores the advantage of temperature control for adjusting the split ratio (as depicted in Figs. 4 and 5) compared with magnetic field control in this system (as shown in Figs. 2 and 3).

In the end, we select $H_1 = 2\,\mathrm{T}$, $H_2 = H_3 = 0\,\mathrm{T}$,

$T_3 = 301\,\mathrm{K}$ and $T_1 = T_2 = 300\,\mathrm{K}$ corresponding to the minimum ratio of 0.15, and study the impact of gap distance on split ratio. By varying the vertical distance d of NP_3 while keeping $l = 8R = 160\,\mathrm{nm}$ [as shown in Fig. 6(a)], or altering the distance l between NP_1 and NP_2 while maintaining $R = 20\,\mathrm{nm}$ [as shown in Fig. 6(b)], the heat flux power P decreases exponentially with increase in the gap distance between NPs.

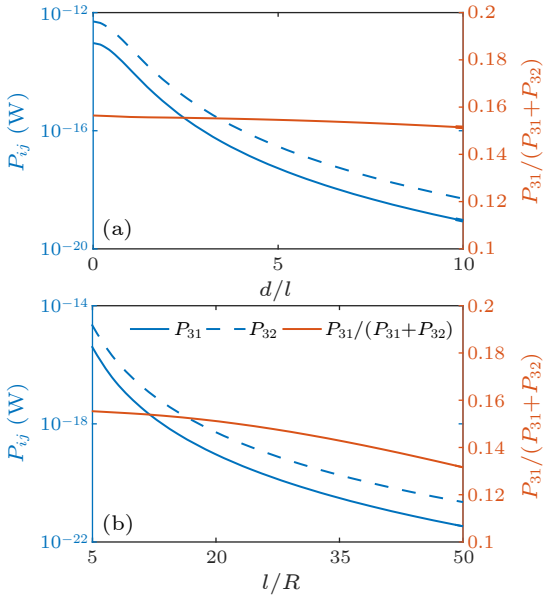

Fig. 6. Left vertical axis: heat flux powers P_{31} (solid blue line) and P_{32} (dashed blue line) (a) versus the vertical distance d of NP_3, while $l = 8R = 160\,\mathrm{nm}$, and (b) versus the distance l between NP_1 and NP_2, while $R = 20\,\mathrm{nm}$. Right vertical axis: corresponding thermal split ratio (orange line). The legend in (b) also applies to (a).

This exponential decrease is a consequence of the near-field radiation of a single particle decreasing with d^3 or l^3. The heat flux power P resulting from dipole interaction follows the relationship $P \propto 1/d^6$ or $P \propto 1/l^6$ in the near-field regime.[14] Then, because both P_{32} and P_{31} decrease synchronously as the gap distance increases, the split ratio $P_{31}/(P_{31}+P_{32})$ changes slightly with the vertical distance d and distance l between NPs. Obviously, this conclusion also applies to the case of the maximum split ratio.

In summary, we have investigated a thermal splitter comprising three magneto-optical InSb NPs, based on the many-body radiative heat transfer theory. Among these particles, NP_3 acts as the source, while NP_1 and NP_2 serve as drains. The main focus is on the system's capability to control the direction of heat flux, i.e., changing the split ratio by adjusting the magnetic field or temperature on the source. Firstly, the magnetic field on NP_1 is fixed, and the magnetic field on NP_3 is varied from 0 to 6 T. The results show a maximum modulation range of the split ratio from 0.15 to 0.58. Analysis of the transmission coefficient reveals that the maximum ratio arises from the coupling between the separated modes on the NPs induced by the magnetic field. Conversely, the minimum ratio is attributed to the suppression of the zero-field mode caused by the magnetic field. However, the presence of coupling between the type-I zero-field modes, whose frequency remains unchanged with the magnetic field, imposes limitations in InSb thermal splitters relying solely on magnetic field modulation. Next, a fixed magnetic field is applied to NP_1, and the impact of temperature variation on the split ratio of NP_3 is examined. Temperature control achieves a significantly enhanced split ratio with a modulation range of 0.15–0.99. Transmission coefficient analysis reveals that the minimum ratio results from zero-field mode suppression induced by the magnetic field. The maximum ratio arises due to the blue shift of mode I supported by NP_3 with increasing temperature, along with its coupling with the separated mode Ⅲ on NP_1. Furthermore, the effect of gap distance on the split ratio is studied. It is observed that the heat flux power decreases exponentially with increase in distance between NPs, resulting in no significant changes in the split ratio with variations in vertical distance d or distance l between the NPs. Compared with thermal splitters based on adjusting a single parameter of graphene or a semimetal, the InSb magneto-optical NP thermal splitter allows for control of the split ratio using both magnetic field and temperature. However, the split ratio of the InSb-based thermal splitter does not achieve the ideal range of 0.01–0.99 due to the weak gyrotropic resonance and the presence of zero-field mode I. Further investigation into the nonlocal effects and rotation effects of InSb NPs will be considered in our future work. Overall, the near-field radiative thermal splitter based on InSb magneto-optical particles expands the potential of InSb for information processing and paves the way for the development of active control over the propagation directions for heat fluxes exchanged in the near-field throughout integrated nanostructure networks.

Acknowledgments. This work was supported by the National Natural Science Foundation of China (Grant Nos. 92050104, 12274314, 12174281, and 52106099), the Natural Science Foundation of Jiangsu Province (Grant No. BK20221240), the Natural Science Foundation of Shandong Province (Grant No. ZR2022YQ57), and the Taishan Scholars Program.

References

[1] Liu R Y, Zhou C L, Zhang Y, Cui Z, Wu X H, and Yi H L 2022 *Int. J. Extreme Manuf.* **4** 032002
[2] Rincón-García L, Thompson D, Mittapally R, Agraït N, Meyhofer E, and Reddy P 2022 *Phys. Rev. Lett.* **129** 145901
[3] Cuevas J C and García-Vidal F J 2018 *ACS Photon.* **5** 3896
[4] Zhu L X, Guo Y, and Fan S H 2018 *Phys. Rev. B* **97** 094302
[5] St-Gelais R, Zhu L, Fan S, and Lipson M 2016 *Nat. Nanotechnol.* **11** 515
[6] Otey C R, Lau W T, and Fan S 2010 *Phys. Rev. Lett.* **104** 154301
[7] Ben-Abdallah P and Biehs S A 2014 *Phys. Rev. Lett.* **112** 044301
[8] Joulain K, Ezzahri Y, Drevillon J, and Ben-Abdallah P 2015 *Appl. Phys. Lett.* **106** 133505

[9] Hu Y, Liu H, Yang B, Shi K, Antezza M, Wu X, and Sun Y 2023 *Phys. Rev. Mater.* **7** 035201
[10] Zhang J H, Liu H T, Zhang K H, Cao J C, and Wu X H 2023 *Int. J. Heat Mass Transfer* **202** 123714
[11] Toyin O R, Ge W, and Gao L 2021 *Chin. Phys. Lett.* **38** 016801
[12] He M J, Qi H, Ren Y T, Zhao Y J, and Antezza M 2019 *Appl. Phys. Lett.* **115** 263101
[13] Fang J L, Qu L, Zhang Y, and Yi H L 2022 *Int. J. Heat Mass Transfer* **190** 122711
[14] Ben-Abdallah P, Belarouci A, Frechette L, and Biehs S A 2015 *Appl. Phys. Lett.* **107** 053109
[15] Song J L, Lu L, Li B W, Zhang B P, Hu R, Zhou X P, and Cheng Q 2020 *Int. J. Heat Mass Transfer* **150** 119346
[16] Guo C, Zhao B, Huang D, and Fan S 2020 *Acs Photon.* **7** 3257
[17] Xu G D, Sun J, Mao H M, and Pan T 2018 *J. Quant. Spectrosc. Radiat. Transfer* **220** 140
[18] Feng D D, Yee S K, and Zhang Z M 2021 *Appl. Phys. Lett.* **119** 181111
[19] Wang K and Gao L 2020 *ES Energy Environ.* **7** 12
[20] Ogundare R T, Ge W, and Gao L 2022 *Opt. Express* **30** 18208
[21] Ben-Abdallah P 2016 *Phys. Rev. Lett.* **116** 084301
[22] Messina R, Ott A, Kathmann C, Biehs S A, and Ben-Abdallah P 2021 *Phys. Rev. B* **103** 115440
[23] Hu Y, Sun Y, Zheng Z, Song J, Shi K, and Wu X 2022 *Int. J. Heat Mass Transfer* **189** 122666
[24] Ott A, Messina R, Ben-Abdallah P, and Biehs S A 2019 *J. Photon. Energy* **9** 1
[25] Lee C S, Lee H, and Westervelt R M 2001 *Appl. Phys. Lett.* **79** 3308
[26] Panina L V, Gurevich A, Beklemisheva A, Omelyanchik A, Levada K, and Rodionova V 2022 *Cells* **11** 950
[27] Liu H T, Shi K Z, Zhou K, Ai Q, Xie M, and Wu X H 2023 *Int. J. Heat Mass Transfer* **208** 124081
[28] Ben-Abdallah P, Biehs S A, and Joulain K 2011 *Phys. Rev. Lett.* **107** 114301
[29] Sun Y S, Hu Y, Shi K Z, Zhang J H, Feng D D, and Wu X H 2022 *Phys. Scr.* **97** 095506
[30] Luo M G, Zhao J M, Liu L H, Guizal B, and Antezza M 2021 *Int. J. Heat Mass Transfer* **166** 120793
[31] Albaladejo S, Gómez-Medina R, Froufe-Pérez L S, Marinchio H, Carminati R, Torrado J F, Armelles G, García-Martín A, and Sáenz J J 2010 *Opt. Express* **18** 3556
[32] Dong J, Zhang W, and Liu L 2021 *Appl. Phys. Lett.* **119** 021104
[33] Moncada-Villa E and Cuevas J C 2020 *Phys. Rev. B* **101** 085411
[34] Moncada-Villa E, Fernández-Hurtado V, García-Vidal F J, García-Martín A, and Cuevas J C 2015 *Phys. Rev. B* **92** 125418